Identifying External Influences on Global Precipitation
Supporting Information

S1 Model Output

We use model output from the 3rd [1] and 5th [2] phases of the Coupled Model Intercomparison Project (CMIP3/5). All data is available for download via the Earth System Grid (see http://cmip-pcmdi.llnl.gov for further information). Tables S2 and S3 list the official acronyms and modeling center information for all models used in this study. In CMIP5, we analyzed:

Historical simulations with estimated changes in anthropogenic and natural forcings over the period 1979-2005 inclusive.

RCP8.5 simulations in which 21st century changes in greenhouse gases and anthropogenic aerosols are prescribed according to the Representative Concentration Pathway 8.5 [3], generally over the period 2005-2012

piControl simulations: pre-industrial runs with no changes in external climate forcings

historicalNat simulations with estimated changes in natural forcings only over the period 1979-2005

Table S4 lists the CMIP5 historical and RCP8.5 simulations used, along with the unique tracking identifier found in the metadata. Table S5 lists the control runs, tracking ids, and the total length of each control run used in this study. To prevent models with longer runs dominating our calculation of internal noise, we use only the first 200 years of every model control simulation.

Of the data available in the CMIP3 archive, we analyzed

Historical simulations with estimated changes in anthropogenic and natural forcings over the period 1979-2000

A1B experiments in which emissions are increased according to Standard Reference Scenario A1B corresponding to a medium-high emissions trajectory [4].

Approximately half of the CMIP3 models include anthropogenic stratospheric ozone depletion as an external climate forcing [5]. These models are indicated in Table S6.

The pre-industrial control runs used do not incorporate changes in external anthropogenic or natural forcings. As such, they provide information about internal variability of the climate system. We have established that the observed trends are very unlikely to result from this internal variability alone, and is consistent with externally forced model results. However, external forcings can be divided into two categories: anthropogenic forcings, such as increased GHG concentrations or stratospheric ozone depletion, and natural forcings due to volcanic activity or solar variability. In order to ascertain the roles of natural and human forcings, we use the CMIP5 historicalNat experiments, which incorporate observed changes in natural external forcings but not anthropogenic contributions. The vast majority of these experiments end in December 2005, meaning we must test 26-year trends over the period 1979-2005. Table S7 lists the historicalNat simulations used in this study.

S2 Splicing

For extended analysis, CMIP5 historical simulations are combined with RCP8.5 runs, and CMIP3 historical simulations with A1B runs. In CMIP5, model metadata are checked and a spliced file is created provided:

- The designated parent experiment of the RCP8.5 run is historical
- The ensemble member identifiers (as defined in the CMIP5 Data Reference Syntax Document) of the RCP8.5 run and indicated parent match
- Historical experiments end in December 2005 (November 2005 for Hadley Centre models)
- RCP8.5 experiments begin January 2006.

Imposing these criteria excludes several available models from the splicing process; those used in this study are listed in Table S4.

S3 Observational Datasets

We used version 2.2 of the Global Precipitation Climatology Project (GPCP) dataset [6], available at http://www.esrl.noaa.gov/psd/data/gridded/data.gpcp.html. This dataset consists of monthly means from January 1979-January 2013. Because we considered boreal winter (DJF) seasonal means and required that all three months be present, we used 33 years of winter mean data. The observational data is gridded to a 2.5x2.5 degree latitude-longitude grid, which is sufficiently highly resolved to detect shifts in the latitudes of zonal mean precipitation features. GPCP is also the most reasonable dataset over ocean [7]. The dataset is believed to be more reliable post-1988, when measurements from the Special Sensor

Microwave Imager (SSM/I, [8]) begin to be incorporated [9]. Figure S1 shows the observed signal-to-noise ratio, calculated from GPCP-derived thermodynamic and dynamic indicators, as a function of the trend start year. Even when the preceding years are excluded from the record, the 1988-2012 trend remains significant at the 95% confidence level.

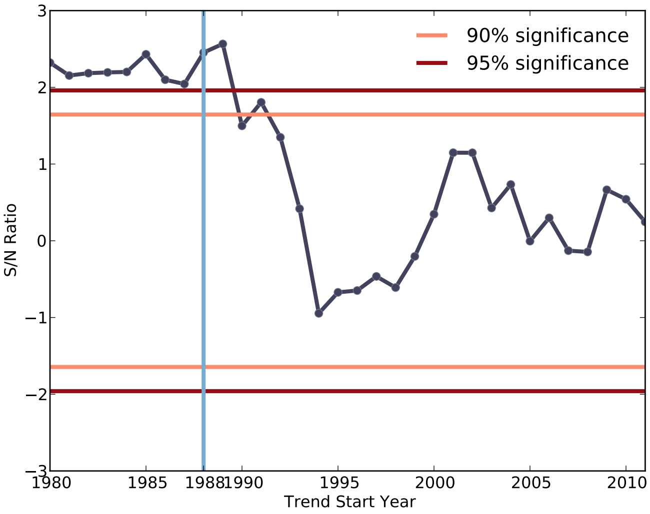

Figure S1: Signal-to-noise ratio as a function of trend start time. All trends end in 2012.

To regress out the effects of ENSO (Section S8), we used the historical monthly Niño 3.4 index (defined as the average sea surface temperature in the region bounded by 5°North-5°South and 170-120°West) available at http://www.cpc.ncep.noaa.gov/data/indices/.

S4 Observed and Modeled Time Series

We apply scale-space smoothing with smoothing parameter 5 degrees to December-February (DJF) seasonal precipitation climatologies. Considering a single season is useful because expected thermodynamic and dynamic trends vary with the seasonal cycle; DJF is chosen because dynamic changes are expected to be largest in boreal winter [5, 10]. The smoothing is performed via diffusion on the sphere as discussed in [11]. This choice of smoothing method removes fine-scale variability, preserves the native model grid, and does not introduce new structure into the map as an artifact of the smoothing procedure. The resulting smoothed fields are then zonally averaged, yielding a simple picture of the latitude structure of global precipitation.

All models have exactly five extrema in the 30-year mean DJF climatology, and most models have exactly five extrema for every individual year. To handle those that do not, we adopt the following procedure: for each model year, if more than five extrema are found, only the three(two) maxima(minima) closest to the maxima(minima) in the 30-year average are retained. Similarly, if fewer than five extrema are found, only those extrema closest to the 30-year mean values are retained; the other points are masked.

S5 Fingerprint Analysis

What is the estimated response of the climate system to external forcing? Various methods exist to determine the fingerprint of climate change (see, e.g.,[12, 13, 14, 15, 16]). We adopt the methods used in e.g. [17], in which the fingerprint is defined as the first empirical orthogonal function (EOF) of the spatiotemporal data matrix that results from averaging the CMIP5 historical/RCP8.5 data, first over an individual model's realizations, if more than one is available, and then over all models. In the case of $D'_H(t)$, the anomalies in the latitudes of local extrema in the zonal average, along with the half-max points, measure the dynamic changes due to natural and externally forced variability. The double average over realizations and models damps internal variability, because manifestations of random natural phenomena such as ENSO are uncorrelated across models. This means that the resulting average $\overline{D'_H(t)}$ in theory measures changes in the locations of extrema resulting primarily from externally forced variability. The same holds for the averaged thermodynamic changes $\overline{T'_H(t)}$, which yields a picture of the response of precipitation intensity to external forcing.

In this paper, the climate change fingerprint is taken to be the first multivariate EOF of $\overline{\tilde{D}'_H(t)}$ (11 spatial dimensions) and $\overline{\tilde{T}'_H(t)}$ (5 spatial dimensions). The tildes indicate that the input time series have been scaled to unit variance before input. The first EOF is then the eigenvector corresponding to the 16x16 covariance matrix obtained by first concatenating $\overline{\tilde{D}'_H(t)}$ and $\overline{\tilde{T}'_H(t)}$ along their spatial dimensions. The expansion coefficients of the first EOF form a time series: the first principal component. These coefficients show how the primary mode of variability oscillates in time.

S6 Single-variable fingerprints

In this section, we calculate the first empirical orthogonal functions (EOF) of the multi-model average $\overline{D'_H(t)}$ and $\overline{T'_H(t)}$ and their corresponding principal components (Fig S2a-d).

Figure S2a shows that in boreal winter the leading dynamic response to external forcing, $F(D)$, is characterized by poleward expansion in both hemispheres, especially in the storm tracks and on the poleward flank of the dry zones, consistent with previous studies, e.g. [18]. The associated principal component shows a positive trend (Figure S2b), indicating that this response is more strongly expressed over time. Figure S2c indicates that the primary thermodynamic response to forcing, denoted $F(T)$, shows the wet-get-wetter, dry-get drier pattern dictated by the Clausius-Clapeyron relation in a warming world. As for the dynamic indicator, the first principal component (Figure S2d) has a positive trend.

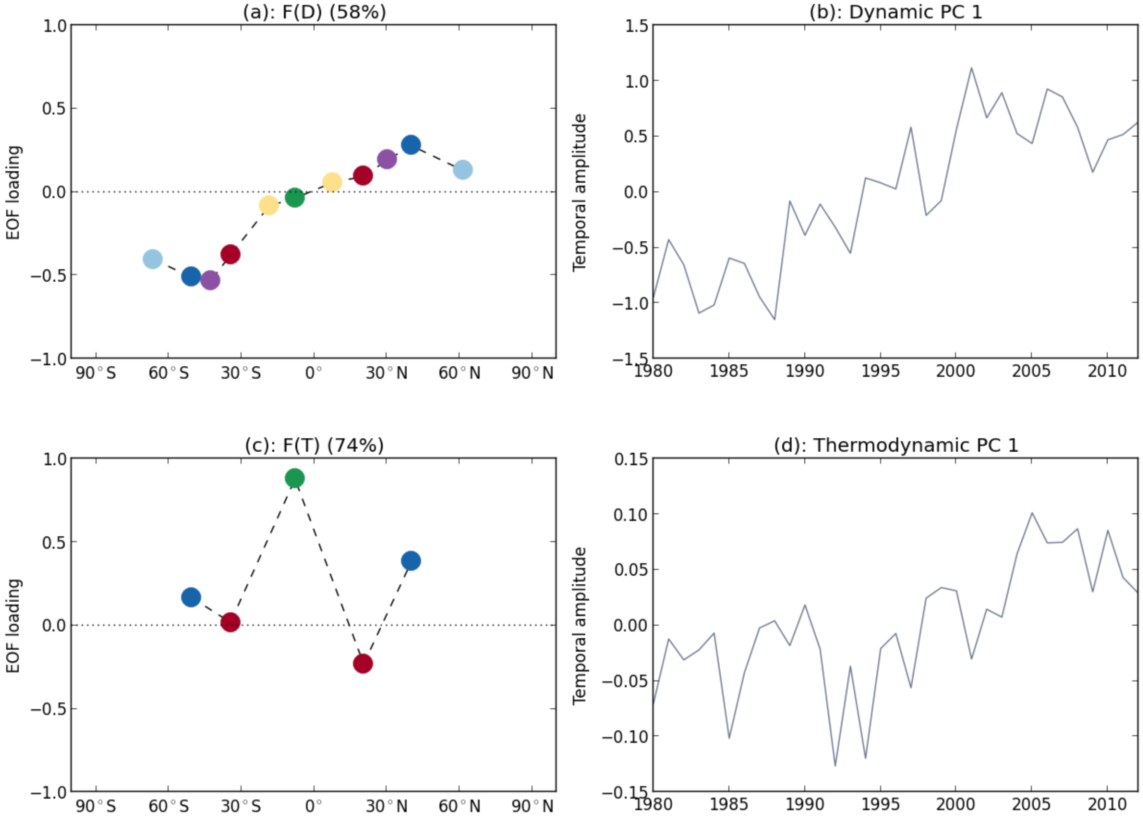

Figure S2: Single-variable fingerprints and first principal components for (a-b): the dynamic indicator $\overline{D'_H(t)}$ and (c-d): the thermodynamic indicator $\overline{T'_H(t)}$.

S6.1 Observed dynamic trends

Figure S3a shows the projection of the *observed* dynamic indicator $D'_O(t)$ onto the fingerprint $F(D)$ and the trend, obtained by least-squares regression. This projection should not be confused with the principal component in Figure S2b, which expresses the strength of the fingerprint in the multimodel average and involves no observational data. The corresponding signal-to-noise ratio, obtained by dividing the trend by the standard deviation of the control distribution, is shown in Figure 3b, as well as fitted probability density functions for the pre-industrial control (blue), ALL5 (green), ALL3 (cyan), and NoOz3 (orange) S/N ratios. As expected, the three forced distributions are offset significantly (Table S1) from the control distribution, which is centered around zero. ALL5 and ALL3 trend distributions do not differ significantly from each other (see Table S1) and are both shifted toward the positive values, indicating that the poleward shift characteristic of $F(D)$ is present in both classes of models. The NoOz3 distribution differs from the ALL3 and ALL5 distribution and has smaller mean trend. This is expected: increased GHG concentrations and stratospheric ozone depletion both contribute to poleward expansion of the general circulation [10, 19, 20] and models that include both forcings will exhibit stronger trends. The observed S/N ratio of 3.83 is significant at the 5% level (Figure S3b). This indicates that the observed trend in the dynamic indicator is very unlikely to result from internal variability alone. However, the observed S/N ratio lies in the far right tail of all three forced distributions, and is thus is also highly unlikely to be compatible with the models' estimate of the dynamic precipitation response to forcing. This is consistent with previous literature, e.g. [5, 21, 22] that suggests the observed expansion of the tropical Hadley cell exceeds model results by an order of magnitude. We therefore detect a dynamic change in precipitation, but are unable to attribute it to any particular forcing or combination of forcings using the current generation of models.

S6.1.1 Comparision with previous studies

Observed dynamic changes appear to be robust across numerous variables such as the jet stream and accompanying storm tracks [23], the Southern Annular Mode [24, 25, 26], the Hadley cell edge calculated from the meridional overturning stream function [27], and the expansion of dry zones determined from zeros of precipitation minus evaporation [28]. These observed dynamic shifts, particularly the widening of the tropical belt, are larger than those predicted by models [5, 21, 22]. This discrepancy between models and observations is not well understood and appears highly sensitive to the metric used [29]. The discrepancy may be due in part to model forcing errors arising from observational uncertainty in ozone changes [30] or to response errors; [31] suggest that models do not accurately capture convective changes in response to warming. Additionally, we find evidence (section S9) that models systematically under-estimate interannual and decadal variability in the dynamic indicator; this means that the model-obtained noise ϵ may be too small and the resulting S/N ratio spuriously inflated. We note, however, that in computing the covariance matrix from which $F_m(D,T)$ is calculated, we normalize $D'_O(t)$ to unit variance, thereby removing the

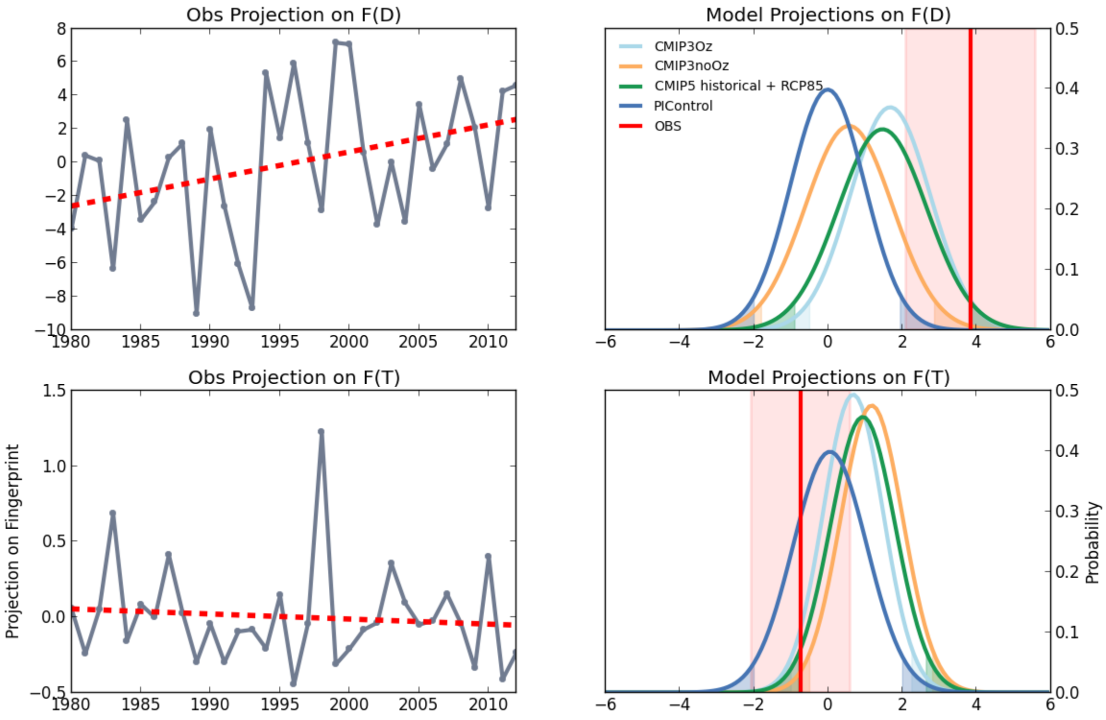

Figure S3: Projection time series and best-fit normal probability distribution functions (PDFs) for trends in the projection of model data onto the fingerprints $F(D)$ (a-b) and $F(T)$ (c-d). In the PDFs, all trends have been normalized by the relevant ϵ, the standard error of the control distribution to obtain signal-to-noise ratios. The blue line shows the PDF of non-overlapping 33-year trends from the concatenated model pre-industrial control runs. The green line shows the PDF for individual CMIP5 historical/RCP8.5 model projection trends. Yellow/cyan lines show the PDF for CMIP3 models excluding/including stratospheric ozone depletion. For all PDFs, the two-sided 95% confidence intervals are shaded. The red line indicates the observed S/N ratio, and the shaded red box ± one standard error in estimating the trend from assumed independent annual samples.

amplitude of variability. Our fingerprint therefore measures the *relationship* between the thermodynamic and dynamic indicators, not their respective amplitudes.

S6.2 Observed thermodynamic trends

Figure S3c shows the projection of the observed thermodynamic indicator $T'_O(t)$ onto the fingerprint $F(T)$. No clear trend is apparent in the time series. Figure S3d shows the S/N ratios for the different classes of model. The ALL3, ALL5, and NoOz3 cases do not differ significantly from each other (Table S1), although they do differ from the control distribution. This is consistent with expected thermodynamic effects: increasing GHG concentrations lead to higher temperatures and an intensification of the hydrological cycle, while ozone depletion alone does not affect precipitation intensity. The observed S/N ratio of -0.8 is compatible with internal variability: we do not detect a thermodynamic change alone.

S6.2.1 Comparison with previous studies

This is not surprising: any mode of natural variability that moistens the tropics or dries the subtropics, ENSO included, will project onto $F(T)$, thereby reducing the signal-to-noise ratio. However, previous studies, e.g. [32, 33], have found that models underestimate the observed strengthening of the hydrological cycle. One possible explanation for the differences between this finding and previous literature is the dataset used. We use observational data from the GPCP dataset, which spans only the satellite era 1979-2012. This time period is shorter than that used in [33, 34] and includes the so-called global warming “hiatus”: the past fifteen years, over which the global temperature rise is significantly slower [35, 36] than that predicted by models [37].

The importance of both dataset and timescale can be seen in Figure S4, which repeats the analysis of [33] using GPCP 1979-2012 data. As in the original paper, annual anomaly data is used (in contrast with our work, which relies on DJF averages), and trends are calculated by zonally averaging and averaging over 10° -wide latitude bands. Anomalies are calculated with respect to the entire 1979-2012 period. The ocean mask used by the CCSM4 CMIP5 land model is re-gridded to the coarser GPCP grid and used to extract observational data over land only. We find that only the northern hemisphere drying trend differs significantly from zero.

Wentz et al [8] use the SSM/I dataset over ocean supplemented with GPCP data to show that the increase in observed precipitation is larger than that predicted by models and scales at roughly the same rate as tropospheric water vapor. Figure 2A in [8] shows an increasing trend in global average precipitation. However, this trend appears to disappear once updated GPCP data is incorporated, as shown in Figure S5, perhaps due to the muted warming trend in recent years.

We also note the low spatial resolution of our thermodynamic indicator: $T'_O(t)$ measures variations at only five spatial points and moistening or drying over large regions is not necessarily captured by changes at a single latitude. Additionally, our study is designed to detect changes in the zonal mean and therefore ignores local changes that may be large in

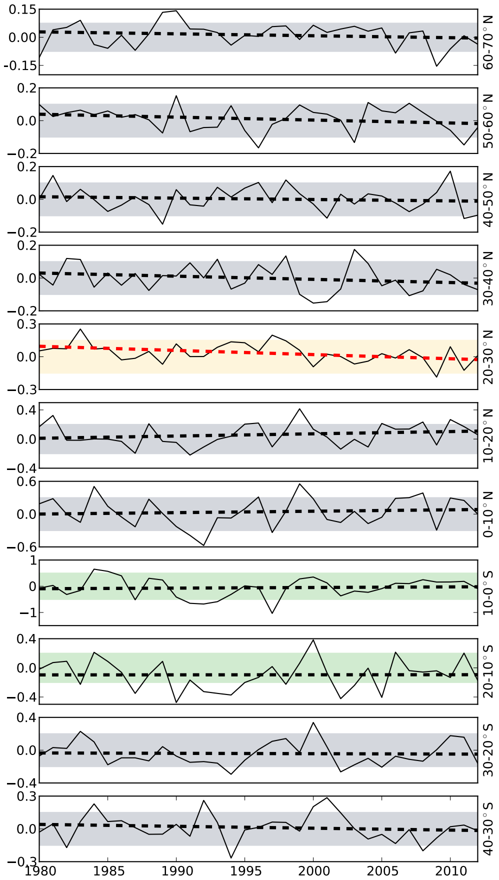

Figure S4: Repeating the analysis of [33] using GPCP data with oceans masked. Time series (black solid lines) are calculated by averaging land-only GPCP data over 10° latitude bands and all longitudes. Green (yellow) shading indicates bands where the trend is positive (negative) and agrees with the trend found by [33]. Gray shading indicates bands where the GPCP trend disagrees with [33]. Dashed lines indicate best-fit trends: red if the trend is significantly different from zero at 95% confidence; black otherwise.

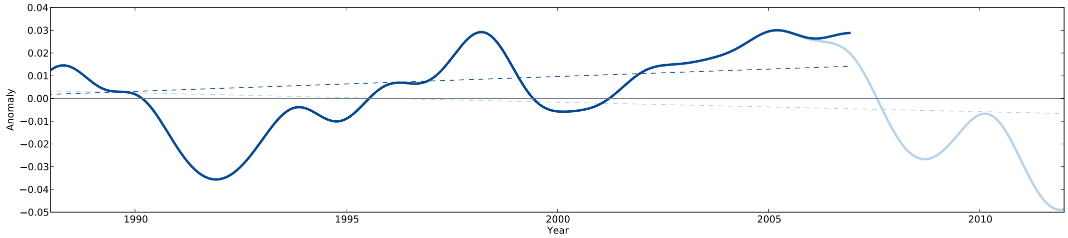

Figure S5: Anomaly time series of global average precipitation for 1988-2006 (dark blue) and 1988-2012 (light blue). As in [8], the seasonal cycle has been removed and data has been smoothed by convolution with a Gaussian distribution of width ± 4 months. The "minimum-norm" constraint [38] has been used at the boundaries, however, trends are not highly sensitive to the boundary conditions chosen. Trends are shown as dashed lines.

magnitude, particularly in the tropics [9]. As shown in Figure S6, the spatial structure of observed DJF precipitation trends in the tropics shows a large east-west gradient. These features, perhaps associated with an observed strengthening of the tropical Walker circulation [39], are averaged over in our methodology.

Natural vs. Anthropogenic Forcing Figure S7 is identical to Figures S3b and d, apart from two changes: trends are now calculated over the 26-period only, and results from model simulations incorporating historical natural forcing only are included. The results for projection onto $F_m(D,T)$ are shown in the main text (Fig 3c). The trend distributions in the historicalNat model runs are nearly identical to those obtained from the pre-industrial control runs, indicating that natural forcing terms (solar variability and volcanic eruptions) do not change the overall distribution.

S7 Relative Frequency Histograms

Figure S8 shows the relative frequency histograms of 33-year trends in CMIP5 control and spliced historical/RCP8.5 runs and in CMIP3 models including and excluding anthropogenic stratospheric ozone depletion. Best-fit normal distributions are shown in Figures S3b, S3d and 3b.

In order to determine whether the observed trends could have been drawn from the same distribution, we performed Kolmogorov-Smirnov tests on all pairs of distributions. The results are summarized in Table S7.

These tests show that:

CMIP3 and CMIP5 are similar. In all cases, the ALL5 trend distributions are statistically indistinguishable (N) from ALL3 trend distributions, indicating that CMIP5 and CMIP3 models that incorporate stratospheric ozone depletion perform similarly.

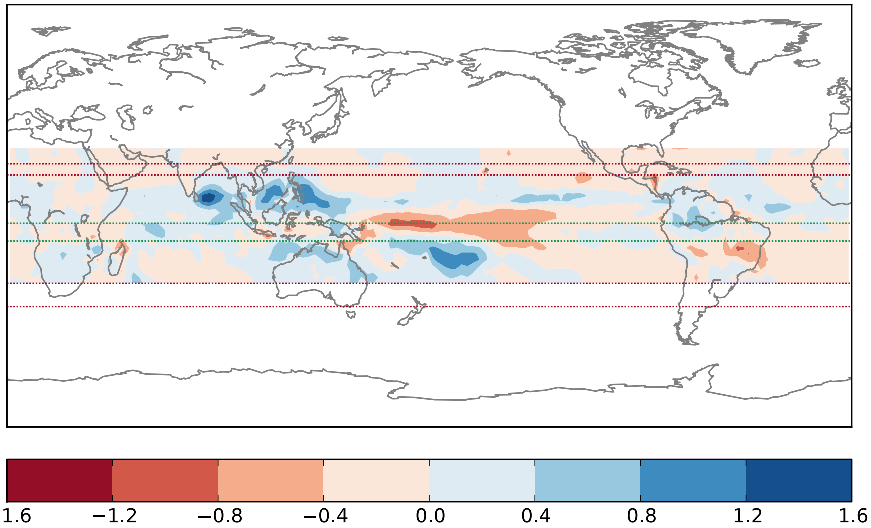

Figure S6: Trends in GPCP DJF average precipitation. Green lines show the range of latitudes identified as tropical peaks at each time step in the zonal average, while red lines show the range of latitudes identified as dry zone troughs in the zonal average. There is a clear east-west pattern in the trends, with drying in the central equatorial Pacific and moistening in the west, consistent with the persistent La Nina-like trend reported by e.g. [40].

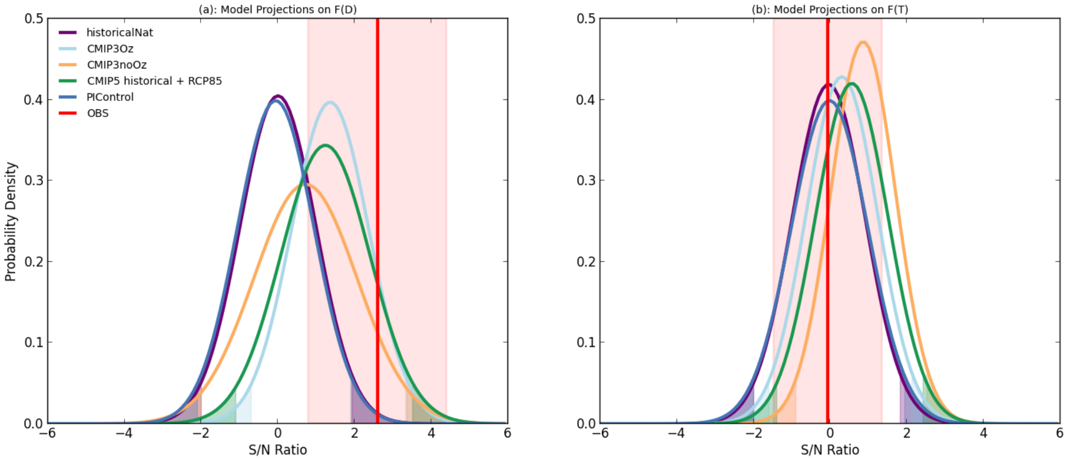

Figure S7: Same as Figure S2b and c, but using 26-year trends and including historicalNat experiments (purple)

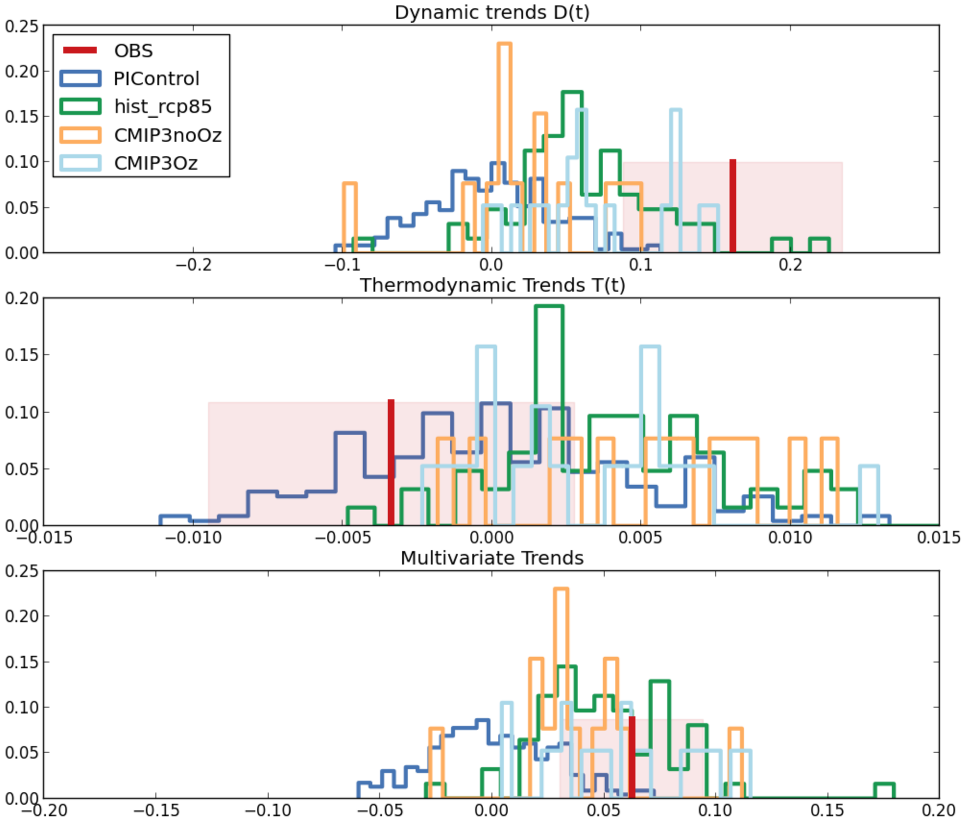

Figure S8: Relative-frequency histograms of 33-year trends in the projection of $D'(t)$ onto $F(D)$(top), $T'(t)$ on to $F(T)$ (middle), and $D'(t)$ and $T'(t)$, scaled to unit variance, onto $F_m(D,T)$ (bottom)

	Control	ALL5	ALL3	NoOz3
Control	—	R***/R***/R***	R***/R***/R***	N/R***/R***
ALL5	R***/R***/R***	—	N/N/N	R**/N/N
ALL3	R***/R***/R***	N/N/N	—	R**/N/N
NoOz3	N/R***/R***	R**/N/N	R**/N/N	—

Table S1: Results of Kolmogorov-Smirnov tests on the CMIP5 control and historical/RCP8.5 trend distributions and CMIP3 models including and excluding anthropogenic stratospheric ozone depletion. Results are reported for distributions of 33-year trends in projections onto $F(D)/F(T)/F_m(D,T)$. An N indicates that we do not reject the hypothesis that the trends are drawn from the same distribution, while R means we reject the null hypothesis with 90% (*), 95% (**), or 99%(***) confidence.

Ozone is important for dynamical shifts. Anthropogenic stratospheric ozone depletion is required to produce positive trends in the projection on $F(D)$. Both the ALL5 and ALL3 trend distributions differ significantly from Control (at the 95% confidence level; R***), while the NoOz3 distribution is statistically indistinguishable from Control (N). The trend distributions also differ between models including (ALL3, ALL5) and excluding (NoOz3) ozone depletion.

External forcings other than ozone depletion are important for thermodynamic changes. For the projection onto $F(T)$, all three forced distributions (ALL5, ALL3, and NoOz3) differ significantly from the control distribution (R***). This suggests, consistent with theory [41, 42], that models that do not include ozone depletion can still produce a thermodynamic response in the hydrological cycle.

The covariance between T and D increases in forced models. All three forced distributions differ significantly from the control distribution of trends in the projection onto the multivariate fingerprint $F_m(D,T)$.

S8 Role of ENSO

In the main text, we contend (Figures 2a and 2c) that ENSO does not project well onto our multivariate fingerprint, and that projection onto $F_m(D,T)$ acts as a passive noise filter. In this section we provide support for that claim. We investigate the role of ENSO, the primary mode of natural variability, by regressing the observed $D'_O(t)$ and $T'_O(t)$ on the observed sea-surface temperature 1979-2012 anomalies in the NINO3.4 region (120° W-170°W and 5°S-5°N) and re-calculating the projection trend with the regression removed to create ENSO-removed indicators $D'_{O,ENSO}(t)$ and $T'_{O,ENSO}(t)$. For the multivariate projection, trends are re-calculated using the ENSO-removed location and intensity time series normalized to unit variance. This provides a fast and simple means of assessing the response of both thermodynamic and dynamic indicators to ENSO variability. Figure S9 show the effect of removing ENSO in this way.

Removing ENSO from $D'_O(t)$ and $T'_O(t)$ individually changes the projection of these indicators onto their respective fingerprints. The trend in the projection of $D'_{O,ENSO}(t)$ onto $F(D)$ is slightly reduced relative to the trend in the raw projection. This indicates that removing ENSO flattens the trend slightly. The projection of $T'_{O,ENSO}(t)$ onto $F(T)$ reduces the size of the 1998 peak, and yields a non-significant positive trend. Both single-variable projection time series are noticeably altered when ENSO effects are regressed out.

When the ENSO-removed indicators are normalized and projected onto the multivariate fingerprint $F_m(D, T)$, however, the result is almost completely unchanged. This provides evidence for our contention that $F_m(D, T)$ acts as an effective noise filter, because the primary noise mode, shown in Figure 2c in the main text, does not project onto the multivariate fingerprint.

S9 Variability

In this section, we compare modeled and observed variability in the projections on D&A studies rely on credible model estimates of internal variability [43, 44]. If models systematically underestimate the amplitude of natural climate noise, this may lead to spurious detection due to artificially low noise, which inflates the S/N ratio. To investigate this possibility, we compare variability in observations and spliced CMIP5 historical/RCP8.5 runs. We first detrend modeled and observed time series of projections onto position $F(D)$ and intensity $F(T)$ fingerprints and then apply a band-pass filter to extract variability on scales between 5 and 20 years, as in [44]. We also apply a high-pass filter to extract variability on scales less than three years. Figure S1 shows the performance of models at simulating medium and high-frequency variability in the projections.

We find:

- Climate models indeed systematically underestimate variability in the projection of the modeled dynamic indicator $D'(t)$ onto the multimodel fingerprint $F(D)$ (Figure S10). This appears to be the case for both short and longer time scales. The multi-model average (white box) lies well in the lower left-hand quadrant.

- For the projection of $T'(t)$ onto the fingerprint $F(T)$, the multi-model average overestimates decadal (5-20 year) variability, and captures observed short-term variability very well (Figure S11). However, there is considerable spread in model performance, with several underestimating variability on both short and long time scales.

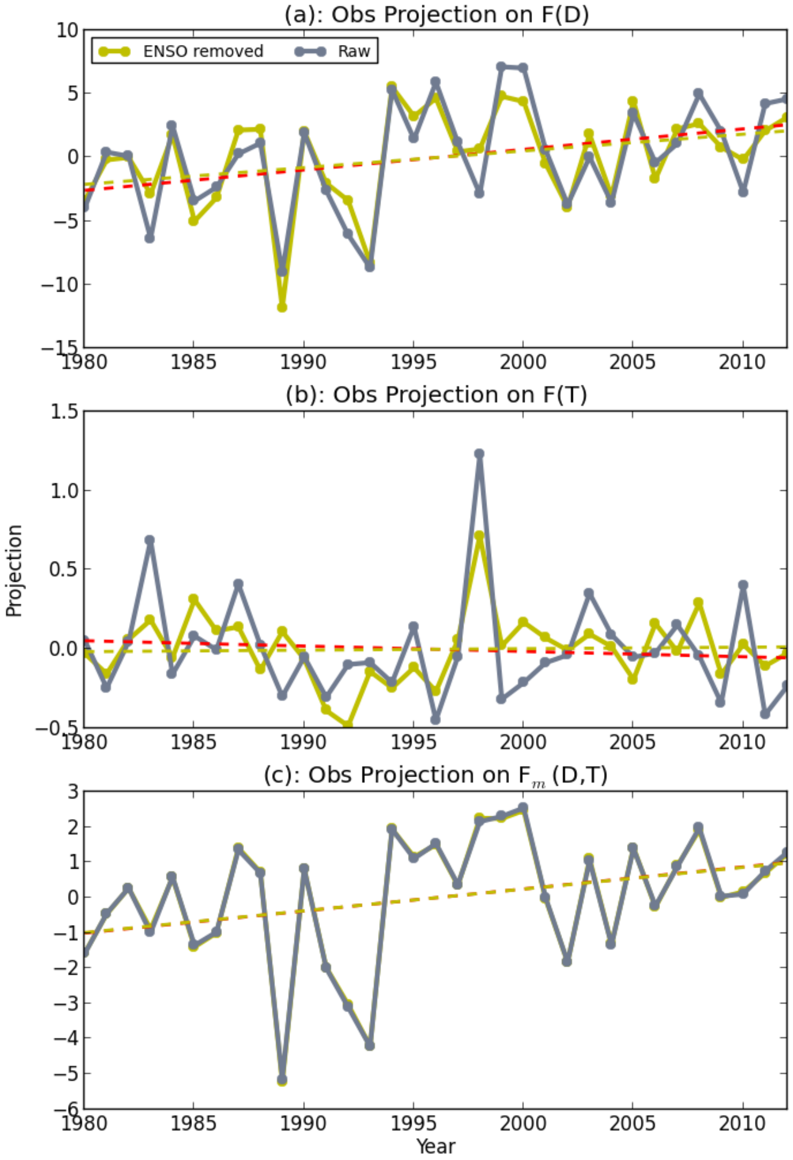

Figure S9: Projections onto the single-variable fingerprints a: $F(D)$, b: $F(T)$, and the multivariate fingerprint $F_m(D,T)$ including time series in which the regression on NINO3.4 SSTs has been removed from the observations.

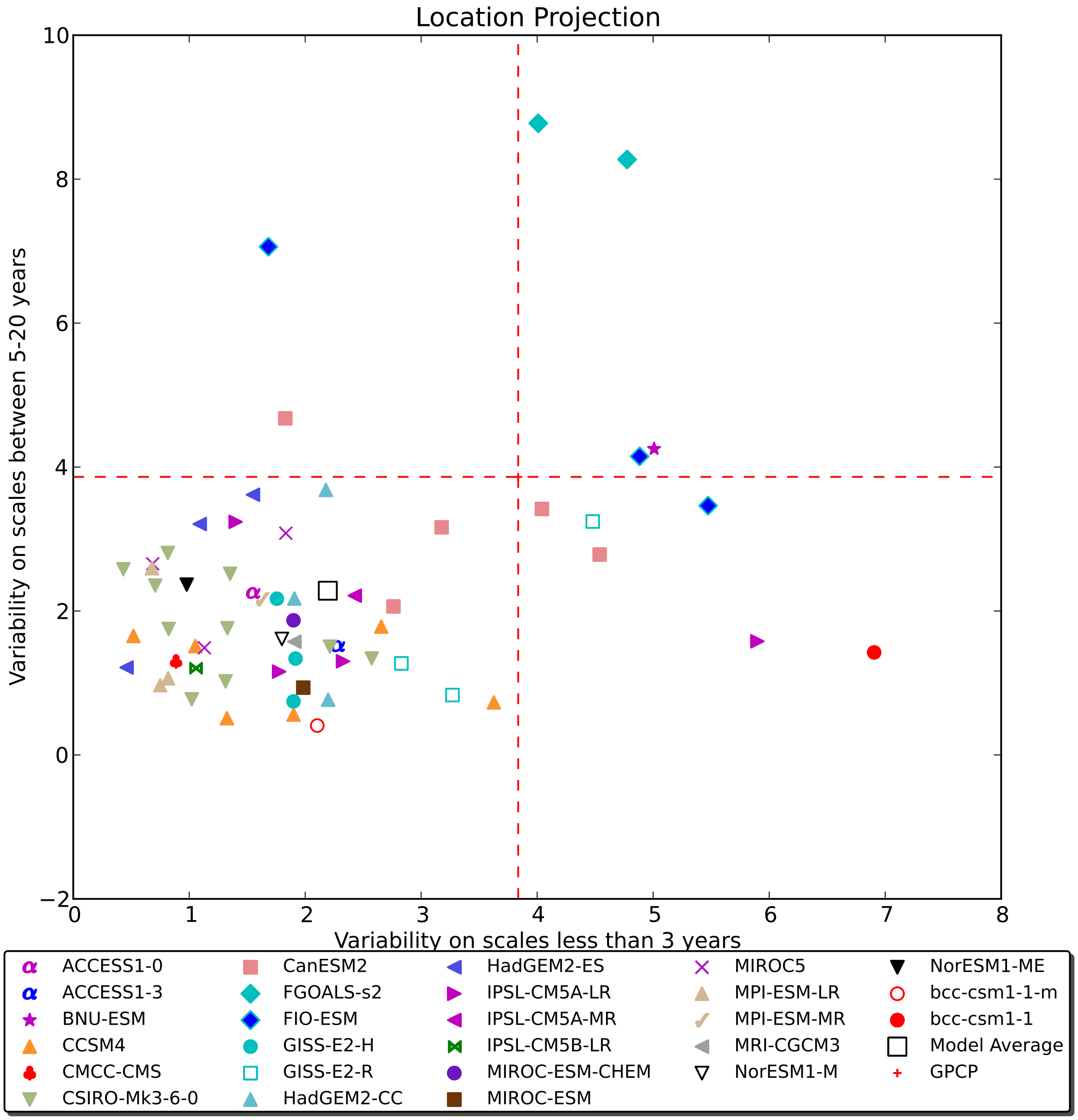

Figure S10: Comparison of modeled and observed variability in the projection of boreal winter mean peak location $D'(t)$ on the fingerprint $F(D)$.

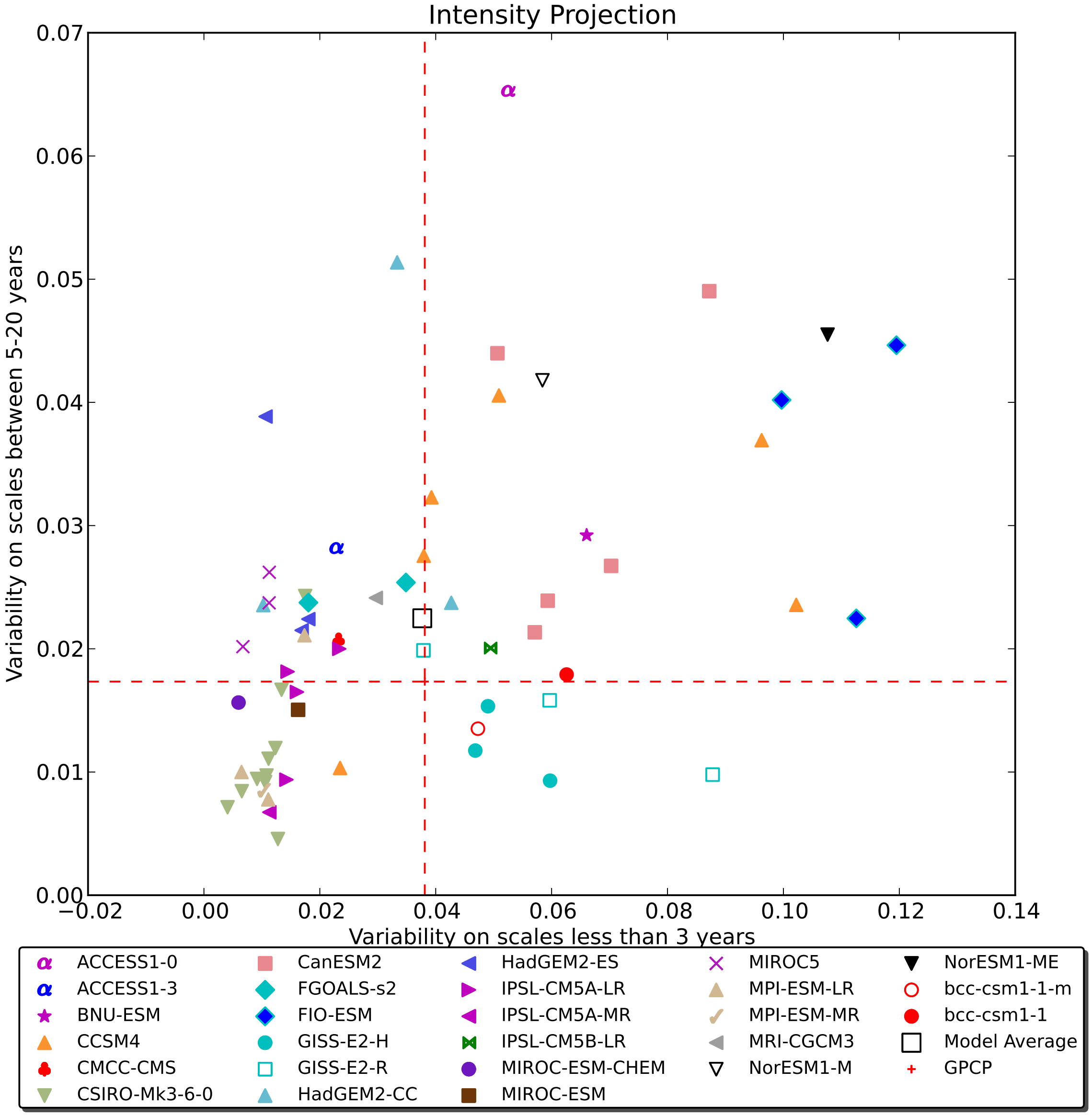

Figure S11: Comparison of modeled and observed variability in the projection of boreal winter mean peak intensity $T'(t)$ on the fingerprint $F(T)$.

Table S2: Official acronyms and modeling center information of the CMIP5 models used in this study.

Model	Country	Modeling Center
ACCESS1-0	Australia	CSIRO (Commonwealth Scientific and Industrial Research Organisation), and BOM (Bureau of Meteorology), version 1.0
ACCESS1-3	Australia	CSIRO (Commonwealth Scientific and Industrial Research Organisation, and BOM (Bureau of Meteorology),version 1.3
bcc-csm1-1	China	Beijing Climate Center(BCC),China Meteorological Administration
bcc-csm1-1-m	China	Beijing Climate Center(BCC),China Meteorological Administration
BNU-ESM	China	College of Global Change and Earth System Science, Beijing Normal University
CanESM2	Canada	Canadian Centre for Climate Modelling and Analysis
CCSM4	USA	NSF/DOE NCAR (National Center for Atmospheric Research) Boulder, CO
CESM1-CAM5-1-FV2	USA	NSF/DOE NCAR (National Center for Atmospheric Research) Boulder, CO
CESM1-WACCM	USA	NSF/DOE NCAR (National Center for Atmospheric Research) Boulder, CO, USA
CMCC-CMS	Italy	CMCC - Centro Euro-Mediterraneo per i Cambiamenti Climatici, Bologna
CNRM-CM5	France	CNRM (Centre National de Recherches Meteorologiques, Meteo-France, Toulouse,France) and CERFACS (Centre Europeen de Recherches et de Formation Avancee en Calcul Scientifique, Toulouse, France)
CSIRO-Mk3-6-0	Australia	Australian Commonwealth Scientific and Industrial Research Organization (CSIRO) Marine and Atmospheric Research (Melbourne, Australia) in collaboration with the Queensland Climate Change Centre of Excellence (QCCCE) (Brisbane, Australia)
EC-EARTH	EU	EC-Earth (European Earth System Model)
FGOALS-g2	China	IAP (Institute of Atmospheric Physics, Chinese Academy of Sciences, Beijing, China) and THU (Tsinghua University)

Continued on next page

Table S2 – continued from previous page

Model	Country	Modeling Center
FGOALS-s2	China	IAP(Institute of Atmospheric Physics),CAS(Chinese Academy of Sciences),Beijing,China
FIO-ESM	China	FIO(The First Institution of Oceanography,SOA,Qingdao,China)
GFDL-CM3	USA	NOAA GFDL(201 Forrestal Rd, Princeton, NJ, 08540)
GFDL-ESM2M	USA	NOAA GFDL(201 Forrestal Rd, Princeton, NJ, 08540)
GISS-E2-H	USA	NASA/GISS (Goddard Institute for Space Studies) New York, NY
GISS-E2-R	USA	NASA/GISS (Goddard Institute for Space Studies) New York, NY
HadGEM2-CC	UK	Met Office Hadley Centre, Fitzroy Road, Exeter, Devon, EX1 3PB, Carbon Cycle configuration (http://www.metoffice.gov.uk)
HadGEM2-ES	UK	Met Office Hadley Centre, Fitzroy Road, Exeter, Devon, EX1 3PB, Earth System Configuration, (http://www.metoffice.gov.uk)
IPSL-CM5A-LR	France	IPSL (Institut Pierre Simon Laplace, Paris), version 5a, low-resolution configuration
IPSL-CM5A-MR	France	IPSL (Institut Pierre Simon Laplace, Paris, version 5a, medium-resolution configuration)
IPSL-CM5B-LR	France	IPSL (Institut Pierre Simon Laplace, Paris, version 5b, low-resolution configuration)
MIROC-ESM	Japan	JAMSTEC (Japan Agency for Marine-Earth Science and Technology, Kanagawa, Japan), AORI (Atmosphere and Ocean Research Institute, The University of Tokyo, Chiba), and NIES (National Institute for Environmental Studies, Ibaraki)
MIROC-ESM-CHEM	Japan	JAMSTEC (Japan Agency for Marine-Earth Science and Technology, Kanagawa, Japan), AORI (Atmosphere and Ocean Research Institute, The University of Tokyo, Chiba), and NIES (National Institute for Environmental Studies, Ibaraki)

Continued on next page

Table S2 – continued from previous page

Model	Country	Modeling Center
MIROC5	Japan	AORI (Atmosphere and Ocean Research Institute, The University of Tokyo, Chiba, Japan), NIES (National Institute for Environmental Studies, Ibaraki, Japan), JAMSTEC (Japan Agency for Marine-Earth Science and Technology, Kanagawa)
MPI-ESM-LR	Germany	Max Planck Institute for Meteorology, low-resolution configuration
MPI-ESM-MR	Germany	Max Planck Institute for Meteorology, medium-resolution configuration
MRI-CGCM3	Japan	MRI (Meteorological Research Institute, Tsukuba)
NorESM1-M	Norway	Norwegian Climate Centre
NorESM1-ME	Norway	Norwegian Climate Centre

Continued on next page

Table S3: Official acronyms and modeling center information of the CMIP3 models used in this study.

Model	Country	Modeling Center
BCCR-BCM2-0	Norway	BCCR (Bjerknes Centre for Climate Research) University of Bergen, Norway (www.bjerknes.uib.no) NERSC (Nansen Environmental and Remote Sensing Center, Norway (www.nersc.no) GFI (Geophysical Institute) University of Bergen),www.gfi.uib.no
CCCMA-CGCM3-1	Canada	CCCma (Canadian Centre for Climate Modelling and Analysis, Victoria, BC)
CCCMA-CGCM3-1-T63	Canada	CCCma (Canadian Centre for Climate Modelling and Analysis, Victoria, BC)
CNRM-CM3	France	CNRM (Centre National de Recherches Meteorologiques, Meteo-France, Toulouse)
CSIRO-MK3-5	Australia	CSIRO (CSIRO Atmospheric Research, Melbourne)
GFDL-CM2-0	USA	NOAA GFDL (US Dept of Commerce / NOAA / Geophysical Fluid Dynamics Laboratory, Princeton, NJ)
GFDL-CM2-1	USA	NOAA GFDL (US Dept of Commerce / NOAA / Geophysical Fluid Dynamics Laboratory, Princeton, NJ)
GISS-AOM	USA	GISS (NASA/Goddard Institute for Space Studies, New York)
IAP-FGOALS1-0-G	P.R. China	IAP(LASG, Institude of Atmospheric Physics, P.O. Box 9804, Beijing 100029)
INGV-ECHAM4	Italy	INGV (National Institute of Geophysics and Volcanology, Bologna)
INMCM3-0	Russia	INM (Iistitute for Numerical Mathematics, Moscow)
MIROC3-2-HIRES	Japan	CCSR/NIES/FRCGC (Center for Climate System Research, Tokyo / National Institute for Environmental Studies, Ibaraki / Frontier Research Center for Global Change, Kanagawa)
MIROC3-2-MEDRES	Japan	CCSR/NIES/FRCGC (Center for Climate System Research, Tokyo / National Institute for Environmental Studies, Ibaraki / Frontier Research Center for Global Change, Kanagawa)

Continued on next page

Table S3 – continued from previous page

Model	Country	Modeling Center
MPI-ECHAM5	Germany	MPI (Max Planck Institute for Meteorology,Hamburg)
NCAR-CCSM3-0	USA	NCAR (National Center for Atmospheric Research, Boulder, CO)

Continued on next page

Table S4: CMIP5 historical and RCP8.5 simulations used in this study, with their tracking IDs.

Model	**EM**	**Tracking ID (historical)**	**Tracking ID (RCP8.5)**
ACCESS1-0	r1i1p1	df41be79-07e9-4303-811f-c9d2de555253	b80b8832-db69-4417-80b2-5905062c0b0e
ACCESS1-3	r1i1p1	26bfc8da-78ff-4b10-9e13-24492c09bb59	1ddaf336-4462-46b0-b8bf-fb0788182796
bcc-csm1-1-m	r1i1p1	9091af95-2ea2-44e7-8d95-b3df204bee3b	c786d745-0811-46cd-9631-f98e11483c72
bcc-csm1-1	r1i1p1	f78ba073-37d9-4337-89e6-0be697f466bd	c486cbf2-7aa5-490d-8ea0-52245dcdb910
BNU-ESM	r1i1p1	7556ea82-127c-4e53-a9af-24a354151e96	6f2e40e4-3ef0-43fd-ad8e-5ed526e5557d
CanESM2	r1i1p1	e1808d37-64ec-4ed2-80a1-cdc14a78ae8a	653bf3cc-fbd9-435e-a291-3b7b51636907
CanESM2	r2i1p1	492544c2-fbc9-4fce-b387-c473a2c2b823	0eb1c34c-7755-4c74-aa42-f84e3aecab6f
CanESM2	r3i1p1	74a7cb0f-9043-4b61-93c6-064f5f1f0275	50e24ecd-02f6-4502-a5c1-04d0bcef4abc
CanESM2	r4i1p1	ffed3ac5-bf02-4251-8fa2-397352697e03	fc74a1c9-0c00-447d-ad3e-d7059334af10
CanESM2	r5i1p1	80a739c8-1ef0-4468-8c7e-9156e2f24492	faaa5419-e76a-4f37-bfb8-e26c51e471eb
CCSM4	r1i1p1	eac78506-c7e5-40e6-92c5-fbc66f8ee568	fcd72455-6f74-4a13-a916-19be949b07c4
CCSM4	r2i1p1	3d32be36-cdfb-4a48-8d5c-d06704972642	177681c4-09a5-4419-a7d3-6e144c223be6
CCSM4	r3i1p1	e9e731ac-8145-451e-b2a1-bba6f4d19812	65cc27fd-aeb7-415e-8723-10960233a8c8
CCSM4	r4i1p1	f4038ee5-f79d-494d-bc71-900d0a6a8163	bfffbe3e-71bd-4299-84dd-1a3bd9bae89c
CCSM4	r5i1p1	c218010d-b693-49e5-9378-8226302fc063	055cb5a3-e86a-4407-b0d1-39730141afc5
CCSM4	r6i1p1	31eebdcc-18f0-4219-b1ff-cd14c7232edd	9edd796b-dd10-4c9a-a4fd-6c4746a40e58
CMCC-CMS	r1i1p1	ca26f36f-e811-4085-877a-7ac0f6a1c452	e17d4913-273b-4c4a-8aef-1530ee3b3284
CSIRO-Mk3-6-0	r10i1p1	7a72e5bd-36ea-40cb-856d-2021ceeb8082	7909bae4-a37f-4cf0-8627-f19349c12b43
CSIRO-Mk3-6-0	r1i1p1	51520639-1698-4708-a08f-4b6acf58394d	a693c52d-2fc3-437d-a9dd-8b0d41e8460e
CSIRO-Mk3-6-0	r2i1p1	c4cd67ba-7bf5-42c1-aa63-546198310017	ff734e88-62f6-4a28-9d02-41d7ca4d6bcc
CSIRO-Mk3-6-0	r3i1p1	2a9f4082-d382-43af-97ba-d73be4a69afb	23bfb6df-c788-42a7-be09-09b4e6e705b1
CSIRO-Mk3-6-0	r4i1p1	8e41d4fd-af04-4c50-bb6a-4443d581c5cc	de97e306-42f9-4889-9f78-b3858ce090ea
CSIRO-Mk3-6-0	r5i1p1	16366ab8-b765-4e16-a26b-72abb8506948	fde6860d-e179-4271-a2fa-ac692bb9a973
CSIRO-Mk3-6-0	r6i1p1	cffab938-c279-4c8a-b850-228e0e1c743d	d1140a1e-ffce-4146-8558-70074089a72b
CSIRO-Mk3-6-0	r7i1p1	c2dbec18-a621-4609-8c45-01f6c2a0c3b2	fe2d8047-0f10-4d73-979c-6faea89e00ea
CSIRO-Mk3-6-0	r8i1p1	d6fa8d41-b119-43c1-bda0-6e061780b37e	93b88165-ee6d-45f4-8bb4-544255ccb5ca
CSIRO-Mk3-6-0	r9i1p1	b20acc5a-1ddb-449d-af4f-f70b75c8fe1d	b2e511c6-34b0-482c-bc52-716a3b352799

Continued on next page

Table S4 – continued from previous page

Model	EM	Tracking ID (historical)	Tracking ID (RCP8.5)
FGOALS-s2	r2i1p1	1f4d2d39-38e1-422d-a053-4adea43a4658	eaf20e1e-b0b8-42bc-97c9-c1dbbbb633a1
FGOALS-s2	r3i1p1	79822584-8c52-4fba-93a0-22c56536f9fa	7a535af6-d516-4738-a2e0-1df064556a60
FIO-ESM	r1i1p1	0166a94a-f2ab-4dd3-bb1e-6b511139909b	406a450e-784c-44ae-9dfd-5141d1b6aa7a
FIO-ESM	r2i1p1	206f07b0-d4cd-4d62-9a8b-974634cf6189	bc2f85dc-2146-47cf-aff7-208a266b964c
FIO-ESM	r3i1p1	47eea2ab-0cc7-4ea1-a41c-5c82816a7bd2	f04cc256-12c5-4255-a8d7-45b8a94c58b8
GISS-E2-H	r1i1p1	4a526154-8c40-4042-a4f2-95ade51683e9	28538783-f3cd-423d-bbe3-81bc56623c27
GISS-E2-H	r1i1p2	d1ec6758-d394-4e93-88a5-d6cb4487c208	df22a560-bd2d-4601-8a20-7dfd16836aad
GISS-E2-H	r1i1p3	cc694480-0b05-4afe-99ff-ed0120d48572	9ca9a1ce-824c-4b55-a2ee-8cf5f45e1568
GISS-E2-R	r1i1p1	76e3b3ec-5319-41ae-96fe-7b65c92e9156	79c8b20e-2088-428e-ba9b-b1f248c6da2c
GISS-E2-R	r1i1p2	df33b26e-80c8-4f49-b509-871ca7e23ce5	0ccc06ba-079f-46b0-9e2b-5cbbb3236c8d
GISS-E2-R	r1i1p3	6f8782a0-0cdd-400a-b446-5ab07f6a74b1	1e79cd98-76ba-4820-acbc-a073ae9a9f05
HadGEM2-CC	r1i1p1	e5d8afbf-a477-4c3e-a9e1-39a25b7a78ad	5d639530-1b3c-4d7a-8bab-1ba07bbe5408
HadGEM2-CC	r2i1p1	96e9adbd-2f3d-4799-8d36-fb5bc2469e2e	1a066ef0-c748-4dbf-98e7-f5adb735901c
HadGEM2-CC	r3i1p1	898afefa-ad0d-40cc-861e-90318eec1519	17e7cc27-d517-4e26-b70b-83fd1dfa8129
HadGEM2-ES	r1i1p1	913a40aa-68f4-49a1-9f31-3baa0dd21819	5705fcfa-d7ce-4511-b005-077580c478c6
HadGEM2-ES	r2i1p1	896c28d8-59a3-45e5-8011-d8cb71371295	772137d0-51ab-47bb-9aa3-8bf3fcc54edb
HadGEM2-ES	r4i1p1	191da815-e604-4e10-b598-44e624db0462	06e9d4cf-ee57-4e86-884e-48a5462925c5
IPSL-CM5A-LR	r1i1p1	ca1f7e92-cda0-44c2-a30b-882b082b2148	eaaefd1f-837a-4883-b186-3fe6af039be7
IPSL-CM5A-LR	r2i1p1	79e179a6-4af7-4376-8c73-7b62164e6031	c338c3ee-738f-46bd-a03f-dff6a1ac05c0
IPSL-CM5A-LR	r3i1p1	ce99797f-166d-46ea-89e5-2ab64f56dcc7	1357fa71-20ff-4ace-b2c6-41bd7ed3df3e
IPSL-CM5A-LR	r4i1p1	13f97ff7-dadb-403e-b684-28ab5292a1ba	8515bbb2-3723-4a26-8443-591c72c8d127
IPSL-CM5A-MR	r1i1p1	2bbc974d-cb9b-47b0-889f-c0abdc6f201a	24fb1076-d7dd-4253-861f-abbb97300d5b
IPSL-CM5B-LR	r1i1p1	2c75cfae-1e9f-412d-96ae-3e173c426b2f	f4241283-dba0-45f1-868e-d6baa9d662f3
MIROC-ESM-CHEM	r1i1p1	486889a5-cd6b-4f93-a6b6-87d541b28c7e	2ff8ca60-0358-4c75-be82-0e569887b8a7
MIROC-ESM	r1i1p1	37cdd6d6-308a-4476-a2b0-448809467c01	84ad336d-7373-41d8-a6ec-c49cdd9867a0
MIROC5	r1i1p1	a906be44-c850-4f0c-b8c4-2b165051669a	c09c0981-a9a3-4a13-a2db-4204f8108609
MIROC5	r2i1p1	b50b70f1-a9c4-4f63-9f8b-d60339913674	ec41e082-357e-46a1-83be-dcae91e14625
MIROC5	r3i1p1	cacb48c2-15ab-420f-91da-c8bb673653bf	6e8cf05d-6bf2-4666-b90f-b237c8aeaacb
MPI-ESM-LR	r1i1p1	00de7790-7297-4bc7-b494-10d2a9727b0d	2c059f4d-4118-4c50-bac7-4d05c3a3af58

Continued on next page

Table S4 – continued from previous page

Model	EM	Tracking ID (historical)	Tracking ID (RCP8.5)
MPI-ESM-LR MPI-ESM-LR	r2i1p1 r3i1p1	b83cbaab-7062-47ac-b978-b02ac72bcba1 5ac7b497-51b3-4070-b004-352956fc42ed	f1765e87-ba94-41b4-8374-85255db69e85 cf89a31e-079b-4d7b-bfd6-d400b935cd08
MPI-ESM-MR	r1i1p1	f94bedfd-180d-43ad-b12d-99f102968059	87fa3a10-89ff-453e-b230-8c29b76bea9e
MRI-CGCM3	r1i1p1	20b61f7b-f6e0-4c53-b6dc-8ddffbb8ecef	e0f6773e-5a70-4e97-9dc2-546ce922b80b
NorESM1-M	r1i1p1	5ccde64e-cfe8-47f6-9de8-9ea1621e7781	22a230b1-5759-45e3-8a40-04b6908be7f0
NorESM1-ME	r1i1p1	8b49fc24-7ff8-4315-bf54-96cedf69f5bf	557a20d8-65b9-415b-a53c-1a037c804102

Table S5: CMIP5 pre-industrial control runs used.

Model	EM	Tracking ID	Control run length (months)
ACCESS1-0	r1i1p1	45165b72-2dd2-4220-bc19-b8ced61957e1	3000
bcc-csm1-1-m	r1i1p1	e00ffb13-a233-48ed-a927-1d334b1191d1	4800
bcc-csm1-1	r1i1p1	e8227cab-28e1-46e5-b848-524a73c454b4	6000
BNU-ESM	r1i1p1	0f152d3c-294a-4d81-b910-112d6f3dc726	6708
CanESM2	r1i1p1	43f9343c-141e-4a0a-a86b-6022b60f0bee	11952
CCSM4	r1i1p1	537336b0-e0f4-4f1c-9ea5-c616db3e1e0f	6012
CCSM4	r2i1p1	77a7f43c-1c47-4eb3-b5f6-1cf3228c621f	1872
CESM1-BGC	r1i1p1	713ec684-49d0-4719-b094-f9bda3aea14e	6000
CESM1-FASTCHEM	r1i1p1	cc64fc83-da1b-4882-804e-572682c9b442	2664
CESM1-WACCM	r1i1p1	f7787226-3c18-4a65-873a-6ca909fb5400	2400
CMCC-CESM	r1i1p1	a66911d4-1a92-47fb-a180-a5ebe521fa34	3324
CMCC-CM	r1i1p1	a14473e0-cba9-4f96-b8cc-65ad12700305	3960
CMCC-CMS	r1i1p1	bd28353c-bb6d-4430-8da1-48c652db2bd5	6000
CNRM-CM5	r1i1p1	31913117-8774-439c-8421-d460db86a306	10200
CSIRO-Mk3-6-0	r1i1p1	679e456b-519a-42ec-b8d2-45107b358483	6000
FGOALS-s2	r1i1p1	f11f0692-cbac-4221-a726-56a01f394d4d	6012
FIO-ESM	r1i1p1	1d0d14df-aa56-4ac0-a698-3c9349bc8b9c	9600
GFDL-CM3	r1i1p1	c6909aeb-77b3-4dc7-a779-a803a3c3a410	6000
GFDL-ESM2G	r1i1p1	0b7417cf-27e8-4983-87ec-db2571ee17ee	6000
GFDL-ESM2M	r1i1p1	3a84b984-747a-4305-b54f-444c862cd564	6000
GISS-E2-H-CC	r1i1p1	1c646280-b2e7-4662-aef8-77167c7c8779	3012
GISS-E2-H	r1i1p1	dd272108-4d6e-43b0-ae79-4b7e357b788d	9360
GISS-E2-H	r1i1p2	241df6c2-8f05-4dc9-bc3e-0c4b5fe07c5e	6372
GISS-E2-H	r1i1p3	8e121eaa-6b13-473d-bdca-8a904617f67c	6372
GISS-E2-R	r1i1p1	4771ae9d-26e7-4ff5-ac17-c96dd7eccbf1	1200
GISS-E2-R	r1i1p141	a058c2ee-5505-4d3d-ae98-73bd622d2c69	13956
GISS-E2-R	r1i1p142	4771ae9d-26e7-4ff5-ac17-c96dd7eccbf1	1200
GISS-E2-R	r1i1p2	5006be04-3af4-4737-a801-8858c2808cee	6372

Continued on next page

Table S5 – continued from previous page

Model	EM	Tracking ID	Control run length (months)
HadGEM2-CC	r1i1p1	e939a08c-0124-4b8e-a860-4668b48c6ebe	2881
HadGEM2-ES	r1i1p1	df32d410-cbf3-400b-b18f-80133f89bf9f	6912
inmcm4	r1i1p1	d3a5f274-0098-48cd-9bb3-b7dfe70b436e	6000
IPSL-CM5A-LR	r1i1p1	c548ab3d-6da6-40fe-8988-af659b74309c	12000
IPSL-CM5A-MR	r1i1p1	beba2e96-6147-44eb-a552-7c884bc1ecb8	3600
MIROC-ESM-CHEM	r1i1p1	6b05dfd5-52ce-4edd-bc2b-cae6bdb9c83b	3060
MIROC5	r1i1p1	61a2f7d3-9c1c-44f1-ae97-04495b4485e7	8040
MPI-ESM-LR	r1i1p1	e12c9ceb-362a-4aab-ab7c-b34cafd3290d	12000
MPI-ESM-P	r1i1p1	5d3051e7-ffe3-4bc3-9548-5507c597a546	13872
MRI-CGCM3	r1i1p1	6c78deac-6f86-4d8a-a183-6b9fa473f062	6000
NorESM1-ME	r1i1p1	c7b4237f-de60-4298-8fd0-1f882d5e42a0	3024

Table S6: List of CMIP3 coupled climate model simulations used

Model	Number of realizations	Includes ozone depletion?
BCCR-BCM2-0	1	No
CCCMA-CGCM3-1	5	No
CCCMA-CGCM3-1-T63	1	No
CNRM-CM3	1	No
CSIRO-MK3-5	1	Yes
GFDL-CM2-0	1	Yes
GFDL-CM2-1	1	Yes
GISS-AOM	2	No
IAP-FGOALS1-0-G	3	No
INGV-ECHAM4	1	Yes
INMCM3-0	1	No
MIROC3-2-HIRES	1	Yes
MIROC3-2-MEDRES	3	Yes
MPI-ECHAM5	4	Yes
NCAR-CCSM3-0	7	Yes

Table S7: CMIP5 historicalNat runs used.

Model	**EM**	**Tracking ID**	**HistoricalNat run length (months)**
bcc-csm1-1	r1i1p1	33009978-4203-4c00-adbd-e80b23399094	1956
BNU-ESM	r1i1p1	1a6b29b1-cf46-4da4-b751-e8d3f6dcee74	1872
CanESM2	r1i1p1	5b2e4672-2c32-4db6-811e-e03e09337559	1956
CanESM2	r2i1p1	2166192d-9be7-4fe3-a711-2ca45974b1e5	1956
CanESM2	r3i1p1	6cf528d0-ccab-4f8b-8b94-5a0a28e9cb56	1956
CanESM2	r4i1p1	90df8edf-2e38-4729-bc5e-69ccaedee9ad	1956
CanESM2	r5i1p1	1f32e147-f052-48bd-9ffe-76b7289fc4ee	1956
CCSM4	r1i1p1	47521ee8-d9cf-498c-a071-dd69e56797c0	1872
CCSM4	r2i1p1	b2854d9f-ac76-427f-8ce9-e0c8da98a3b4	1872
CCSM4	r4i1p1	8ad7ce45-565c-4e6c-bc59-76c021e766a4	1872
CCSM4	r6i1p1	899bad47-f539-40ac-8784-ef340b34fd18	1872
CESM1-CAM5-1-FV2	r3i1p1	caaa3ec0-7efc-417e-b8ad-759ae88342e5	1872
CESM1-CAM5-1-FV2	r4i1p1	97118574-c6b9-4f91-bbd2-a5b12bdb74c3	1872
CNRM-CM5	r1i1p1	5db133b4-be65-4653-89ba-0f00a7dee832	1956
CNRM-CM5	r2i1p1	8a6b1e65-83d7-462d-9c78-fe9e18281502	1956
CNRM-CM5	r3i1p1	cadaeed1-195f-4f40-9281-769aadebe942	1956
CNRM-CM5	r4i1p1	1a80c989-135f-409e-8b63-51554aaf6df1	1956
CNRM-CM5	r5i1p1	46556fb6-aefb-4141-a717-2ca6f5f30e40	1956
CNRM-CM5	r8i1p1	6ff1024c-f7f6-4dc6-a96e-4ac1f22c86a4	1956
CSIRO-Mk3-6-0	r1i1p1	fb18df28-e176-4a10-9fab-2db7d5bb7212	1956
CSIRO-Mk3-6-0	r2i1p1	33692d3d-74c5-4cd3-bd46-906e38b14b4c	1956
CSIRO-Mk3-6-0	r3i1p1	49b2919c-2e7f-4384-a372-edb49adac8ed	1956
CSIRO-Mk3-6-0	r4i1p1	962dd1cb-44aa-4669-b905-f000a3675911	1956
CSIRO-Mk3-6-0	r5i1p1	b7a18f85-6dab-4565-a10b-0abf8594d588	1956
GFDL-CM3	r1i1p1	a378d727-04fa-4626-b7b6-1d4a1089a041	1752
GFDL-CM3	r3i1p1	027f391d-d6cd-4887-997e-66f6ecd31fed	1752
GFDL-CM3	r5i1p1	0b3a9c71-3406-450a-bce6-1ac8290e3cdf	1752
GFDL-ESM2M	r1i1p1	ed314c0c-01f0-48af-b9e4-d8a4ad534db8	1740

Continued on next page

Table S7 – continued from previous page

Model	EM	Tracking ID	HistoricalNat run length (months)
GISS-E2-H	r1i1p1	e57ddff4-5263-484e-8ca5-4cad3798252d	1956
GISS-E2-H	r2i1p1	9228646e-58cf-4631-b63b-84789b7ff09d	1956
GISS-E2-H	r3i1p1	7dc3cd32-fece-4eb1-b1e9-4f4b6f9e2e89	1956
GISS-E2-H	r4i1p1	f793a225-0299-4ac3-b031-438e64212f39	1956
GISS-E2-H	r5i1p1	35a7b1e9-1a5e-4294-9340-b3cb581040b3	1956
GISS-E2-R	r1i1p1	8f4967cd-39c3-4079-b032-451e5092f5f8	1956
GISS-E2-R	r1i1p3	444910a5-7959-4484-8367-069ed0236b44	1956
GISS-E2-R	r2i1p1	de5f27c4-302e-4d2e-9b6a-02e2da2c9ba7	1956
GISS-E2-R	r2i1p3	677786ee-48cd-407e-842e-0bcfdf417093	1956
GISS-E2-R	r3i1p1	c33293ce-df08-4a67-bd7c-5fa3e4968532	1956
GISS-E2-R	r3i1p3	6fb681b3-2ced-4e89-9739-db09e1bcf290	1956
GISS-E2-R	r4i1p1	8c1d5dbd-a415-44f6-8dd3-3e7788c6c583	1956
GISS-E2-R	r4i1p3	bc0ffbff-c610-4db9-9636-7880a021189d	1956
GISS-E2-R	r5i1p1	7db601a4-fd9a-46dc-a083-f7fc78a1747e	1956
GISS-E2-R	r5i1p3	cd3d1e19-3e7b-4c2f-8d4a-bf120feefffe	1956
HadGEM2-ES	r1i1p1	4d31b005-5993-4de7-b230-ec6454d40055	1920
HadGEM2-ES	r2i1p1	ddec24d0-394d-4e7f-bdb4-d5fe855e73a8	1921
HadGEM2-ES	r3i1p1	cea7eaf1-f362-4558-9f08-ac38ab48c02c	1920
HadGEM2-ES	r4i1p1	deb91742-6d9b-41b8-a35a-5ac8e9169956	1921
IPSL-CM5A-LR	r1i1p1	fe3e40dc-8954-4370-a4ea-3ccc3f33a329	1956
IPSL-CM5A-LR	r2i1p1	091c6929-8edf-4ef7-84dc-b425b6134013	1956
IPSL-CM5A-LR	r3i1p1	2b6eeea8-a940-415e-8d69-ea64df040bad	1956
IPSL-CM5A-MR	r1i1p1	8246ee3f-c1fe-4822-942f-5a408af34390	1956
IPSL-CM5A-MR	r2i1p1	52b8b7b4-25fd-4995-8ee4-5583ab16ccbd	1956
IPSL-CM5A-MR	r3i1p1	842615d4-3b84-45e3-81b4-9bb26460839f	1956
MIROC-ESM-CHEM	r1i1p1	a7894ab5-e60e-48f2-bc0c-cca1e1532f7f	1872
MIROC-ESM	r1i1p1	44ffc7bf-6c1a-4c57-b246-5f544a544972	1872
MIROC-ESM	r2i1p1	0c1c2b27-fa64-4ef4-b22b-5adc1b55273d	1872
MIROC-ESM	r3i1p1	8ca0cb25-8787-4e91-afdc-26bbe28d0297	1872

Continued on next page

Table S7 – continued from previous page

Model	EM	Tracking ID	HistoricalNat run length (months)
MRI-CGCM3	r1i1p1	f495cc5a-4332-470a-8e4a-d2cc1b629cb6	1872
NorESM1-M	r1i1p1	7152b5a2-e51d-4a4d-8367-514f6932eadd	1956

References

[1] Meehl, G, Covey, C, Delworth, T, Latif, M, McAvaney, B, Mitchell, J, Stouffer, R, & Taylor, K. (2007) The wcrp cmip3 multi-model dataset: A new era in climate change research. *Bulletin of the American Meteorological Society* **88**, 1383–1394.

[2] Taylor, K. E, Stouffer, R. J, & Meehl, G. A. (2012) An overview of cmip5 and the experiment design. *Bulletin of the American Meteorological Society* **93**, 485–498.

[3] Van Vuuren, D. P, Edmonds, J, Kainuma, M, Riahi, K, Thomson, A, Hibbard, K, Hurtt, G. C, Kram, T, Krey, V, Lamarque, J.-F, et al. (2011) The representative concentration pathways: an overview. *Climatic Change* **109**, 5–31.

[4] Nakicenovic, N, Alcamo, J, Davis, G, de Vries, B, Fenhann, J, Gaffin, S, Gregory, K, Grubler, A, Jung, T. Y, Kram, T, et al. (2000) Special report on emissions scenarios: a special report of working group iii of the intergovernmental panel on climate change, (Pacific Northwest National Laboratory, Richland, WA (US), Environmental Molecular Sciences Laboratory (US)), Technical report.

[5] Min, S.-K & Son, S.-W. (2013) Multi-model attribution of the southern hemisphere hadley cell widening: Major role of ozone depletion. *Journal of Geophysical Research: Atmospheres*.

[6] Adler, R. F, Huffman, G. J, Chang, A, Ferraro, R, Xie, P.-P, Janowiak, J, Rudolf, B, Schneider, U, Curtis, S, Bolvin, D, et al. (2003) The version-2 global precipitation climatology project (gpcp) monthly precipitation analysis (1979-present). *Journal of Hydrometeorology* **4**, 1147–1167.

[7] Yin, X, Gruber, A, & Arkin, P. (2004) Comparison of the gpcp and cmap merged gauge-satellite monthly precipitation products for the period 1979-2001. *Journal of Hydrometeorology* **5**, 1207–1222.

[8] Wentz, F. J, Ricciardulli, L, Hilburn, K, & Mears, C. (2007) How much more rain will global warming bring? *Science* **317**, 233–235.

[9] Allan, R. P, Soden, B. J, John, V. O, Ingram, W, & Good, P. (2010) Current changes in tropical precipitation. *Environmental Research Letters* **5**, 025205.

[10] Polvani, L. M, Waugh, D. W, Correa, G. J, & Son, S.-W. (2011) Stratospheric ozone depletion: The main driver of twentieth-century atmospheric circulation changes in the southern hemisphere. *Journal of Climate* **24**, 795–812.

[11] Marvel, K, Ivanova, D, & Taylor, K. (2013) Scale space methods for climate model analysis. *Journal of Geophysical Research: Atmospheres*.

[12] Allen, M & Stott, P. (2003) Estimating signal amplitudes in optimal fingerprinting, part i: Theory. *Climate Dynamics* **21**, 477–491.

[13] Gillett, N, Zwiers, F, Weaver, A, Hegerl, G, Allen, M, & Stott, P. (2002) Detecting anthropogenic influence with a multi-model ensemble. *Geophysical Research Letters* **29**, 31–1.

[14] Hegerl, G. C, voN SToRcH, H, Hasselmann, K, Santer, B. D, Cubasch, U, & Jones, P. D. (1996) Detecting greenhouse-gas-induced climate change with an optimal fingerprint method. *Journal of Climate* **9**, 2281–2306.

[15] Stott, P. A, Tett, S, Jones, G, Allen, M, Mitchell, J, & Jenkins, G. (2000) External control of 20th century temperature by natural and anthropogenic forcings. *Science* **290**, 2133–2137.

[16] Tett, S. F, Jones, G. S, Stott, P. A, Hill, D. C, Mitchell, J. F, Allen, M. R, Ingram, W. J, Johns, T. C, Johnson, C. E, Jones, A, et al. (2002) Estimation of natural and anthropogenic contributions to twentieth century temperature change. *Journal of Geophysical Research* **107**, 4306.

[17] Santer, B. D, Painter, J. F, Mears, C. A, Doutriaux, C, Caldwell, P, Arblaster, J. M, Cameron-Smith, P. J, Gillett, N. P, Gleckler, P. J, Lanzante, J, et al. (2013) Identifying human influences on atmospheric temperature. *Proceedings of the National Academy of Sciences* **110**, 26–33.

[18] Scheff, J & Frierson, D. M. (2012) Robust future precipitation declines in cmip5 largely reflect the poleward expansion of model subtropical dry zones. *Geophysical Research Letters* **39**.

[19] Deser, C & Phillips, A. S. (2009) Atmospheric circulation trends, 1950-2000: The relative roles of sea surface temperature forcing and direct atmospheric radiative forcing. *Journal of Climate* **22**, 396–413.

[20] Fyfe, J, Gillett, N, & Marshall, G. (2012) Human influence on extratropical southern hemisphere summer precipitation. *Geophysical Research Letters* **39**.

[21] Johanson, C. M & Fu, Q. (2009) Hadley cell widening: Model simulations versus observations. *Journal of Climate* **22**, 2713–2725.

[22] Seidel, D. J, Fu, Q, Randel, W. J, & Reichler, T. J. (2007) Widening of the tropical belt in a changing climate. *Nature Geoscience* **1**, 21–24.

[23] Archer, C. L & Caldeira, K. (2008) Historical trends in the jet streams. *Geophysical Research Letters* **35**.

[24] Fogt, R. L, Perlwitz, J, Monaghan, A. J, Bromwich, D. H, Jones, J. M, & Marshall, G. J. (2009) Historical sam variability. part ii: Twentieth-century variability and trends from reconstructions, observations, and the ipcc ar4 models*. *Journal of Climate* **22**, 5346–5365.

[25] Marshall, G. J. (2003) Trends in the southern annular mode from observations and reanalyses. *Journal of Climate* **16**, 4134–4143.

[26] Thompson, D. W, Wallace, J. M, & Hegerl, G. C. (2000) Annular modes in the extratropical circulation. part ii: Trends. *Journal of Climate* **13**, 1018–1036.

[27] Hu, Y, Fu, Q, et al. (2007) Observed poleward expansion of the hadley circulation since 1979. *Atmos. Chem. Phys* **7**, 5229–5236.

[28] Previdi, M & Liepert, B. G. (2007) Annular modes and hadley cell expansion under global warming. *Geophysical Research Letters* **34**.

[29] Davis, S. M & Rosenlof, K. H. (2012) A multidiagnostic intercomparison of tropical-width time series using reanalyses and satellite observations. *Journal of Climate* **25**, 1061–1078.

[30] Solomon, S, Young, P. J, & Hassler, B. (2012) Uncertainties in the evolution of stratospheric ozone and implications for recent temperature changes in the tropical lower stratosphere. *Geophysical Research Letters* **39**.

[31] Grassi, B, Redaelli, G, Canziani, P. O, & Visconti, G. (2012) Effects of the pdo phase on the tropical belt width. *Journal of Climate* **25**, 3282–3290.

[32] Polson, D, Hegerl, G. C, Zhang, X, & Osborn, T. J. (2013) Causes of robust seasonal land precipitation changes. *Journal of Climate*.

[33] Zhang, X, Zwiers, F. W, Hegerl, G. C, Lambert, F. H, Gillett, N. P, Solomon, S, Stott, P. A, & Nozawa, T. (2007) Detection of human influence on twentieth-century precipitation trends. *Nature* **448**, 461–465.

[34] Noake, K, Polson, D, Hegerl, G, & Zhang, X. (2012) Changes in seasonal land precipitation during the latter twentieth-century. *Geophysical Research Letters* **39**.

[35] Easterling, D. R & Wehner, M. F. (2009) Is the climate warming or cooling? *Geophysical Research Letters* **36**.

[36] Foster, G & Rahmstorf, S. (2011) Global temperature evolution 1979–2010. *Environmental Research Letters* **6**, 044022.

[37] Fyfe, J. C, Gillett, N. P, & Zwiers, F. W. (2013) Overestimated global warming over the past 20 years. *Nature Climate Change* **3**, 767–769.

[38] Mann, M. E. (2004) On smoothing potentially non-stationary climate time series. *Geophysical Research Letters* **31**.

[39] LHeureux, M. L, Lee, S, & Lyon, B. (2013) Recent multidecadal strengthening of the walker circulation across the tropical pacific. *Nature Climate Change* **3**, 571–576.

[40] Kosaka, Y & Xie, S.-P. (2013) Recent global-warming hiatus tied to equatorial pacific surface cooling. *Nature* **501**, 403–407.

[41] Allen, M. R & Ingram, W. J. (2002) Constraints on future changes in climate and the hydrologic cycle. *Nature* **419**, 224–232.

[42] Held, I. M & Soden, B. J. (2006) Robust responses of the hydrological cycle to global warming. *Journal of Climate* **19**, 5686–5699.

[43] Allen, M. R & Tett, S. F. (1999) Checking for model consistency in optimal fingerprinting. *Climate Dynamics* **15**, 419–434.

[44] Santer, B, Mears, C, Doutriaux, C, Caldwell, P, Gleckler, P, Wigley, T, Solomon, S, Gillett, N, Ivanova, D, Karl, T, et al. (2011) Separating signal and noise in atmospheric temperature changes: The importance of timescale. *Journal of Geophysical Research: Atmospheres (1984–2012)* **116**.